Embedded gallium oxide-silica composites in silica matrix via sol-gel process

F. Ramírez-González[a,*], R. A. Vázquez-Sánchez[b], R. Herrera-Rivera[c], J. Conde[a], and H. Vilchis Bravo[d],

[a]*SECIHTI-Instituto de Investigación e Innovación en Energías Renovables, Universidad de Ciencias y Artes de Chiapas, Libramiento Norte 1150 Col. Lajas Maciel, 29039, Tuxtla Gutiérrez, Chiapas, México,*
e-mail: francisco.ramirez@unicach.mx; jorge.conde@unicach.mx
https://orcid.org/0000-0002-0132-4619

[b]*Facultad de Ingeniería, Universidad de Ciencias y Artes de Chiapas, Libramiento Norte 1150 Col. Lajas Maciel, 29039, Tuxtla Gutiérrez, Chiapas, México,*
e-mail: ruben.vazquez@unicach.mx
https://orcid.org/0009-0009-3835-8300

[c]*Facultad de Ciencias Físico-Matemáticas, Universidad Autónoma de Nuevo León, San Nicolás de los Garza, 66451 Nuevo León, México,*
e-mail: maria.herrerav@uanl.edu.mx
https://orcid.org/0000-0003-3629-4525

[d]*Instituto de Investigación e Innovación en Energías Renovables, Universidad de Ciencias y Artes de Chiapas, Libramiento Norte 1150 Lajas Maciel, 29039, Tuxtla Gutiérrez, Chiapas, México,*
e-mail: heber.vilchis@unicach.mx
https://orcid.org/0000-0001-6042-9851

Received 1 January 2022; accepted 9 February 2022

This work reports the synthesis of a gallium oxide (Ga_2O_3)-silica composite within a silica matrix via a modified sol-gel process, with the novelty residing in the incorporation of Ga_2O_3 during the condensation stage. In conventional sol-gel synthesis of silica matrices or nanoparticles, ethanol and tetraethyl orthosilicate (TEOS) are mixed prior to hydrolysis, followed by a distinct condensation step. Typically, the incorporation of a second material into a silica matrix, such as micro- or nanoparticles, is carried out in a separate step using techniques like spray pyrolysis, chemical vapor deposition (CVD), or sputtering. In contrast, the present approach enables the formation of a Ga_2O_3 -silica composite during the condensation step, thereby eliminating the need for post-synthesis deposition methods. This is achieved by introducing a Ga_2O_3 suspension into the TEOS solution prior to hydrolysis. Samples were fabricated by dropcasting both standard and modified sols onto glass substrates, with each layer formed by three successive drops. The functionalization and structural characteristics of the resulting materials were analyzed using X-ray diffraction (XRD), micro-Raman spectroscopy, scanning electron microscopy (SEM), and electrostatic force microscopy (EFM). These characterization techniques confirmed the successful integration of Ga_2O_3 within the silica matrix. In particular, EFM measurements distinguished between silica and Ga_2O_3 domains based on surface charge amplitude. The results demonstrate that both the Ga_2O_3 concentration in the colloidal suspension and the number of deposited layers significantly influence the addition of the crystalline structure of Ga_2O_3 into the silica matrix and its morphology. This simple modification to the sol-gel method is proposed as a general and scalable strategy for the synthesis of metal oxide-silica composites and the functionalization of silica-based materials.

Keywords: Electrostatic force microscope; gallium oxide; silica composites; sol-gel; tetraethyl orthosilicate.

DOI: https://doi.org/10.31349/RevMexFis.72.041008

1. Introduction

Silica composites and related materials have been proposed for applications such as catalysis, adsorption, sensing, healthcare, water treatment, and nanotechnology, due to the addition of micro- or nanoparticles, combining the properties of silica and the other material, either organic or inorganic [1]. Usually, the fabrication of silica-based composites involves two steps. First, the synthesis of silica using a method as hydrothermal or sol-gel, then the material to be combined is added in a second step through a second method of deposition, such as spray-pyrolysis, CVD, or sputtering [2–4]. TEOS is a key precursor in silica formation and is widely utilized in the fabrication of advanced materials, ranging from nanocomposite arrays to optical and electronic devices [5, 6]. The sol-gel (solution-gelation) process is commonly employed to synthesize silica and doped silica materials for diverse applications, such as stabilizing natural pigments [7], aiding in semiconductor synthesis [8], serving as a matrix for nanocomposites [9], creating coatings [10], enabling drug delivery systems [11], and developing flexible supercapacitors [12]. The synthesis and growth of silica particles using TEOS (Si(OC2H5)4) as a silica source involves the reactions in Eqs. (1), (2), and (3), hydrolysis and condensation [13].

$$Si(OC_2H_5)_4 + {}_4H_2O \rightarrow Si(OH_4) + 4C_2H_5OH\ , \quad (1)$$

$$Si(OH)_4 + Si(OC_2H_5)_4 \rightarrow Si\text{-}O\text{-}Si + 4C_2H_5OH\ , \quad (2)$$

$$Si(OH)_4 + Si(OH)_4 \rightarrow Si\text{-}O\text{-}Si + 4H_2O\ . \quad (3)$$

Through these reactions, silica particles are formed as the TEOS undergoes progressive polymerization, leading to the formation of silica particles or a silica matrix. The control of the reaction medium influences the relative rates of hydrolysis and condensation in the synthesis of silica-based materials via the sol-gel method, where a solvent, such as ethanol, can be used to facilitate the hydrolysis reaction [14]. On the other hand, gallium oxide (Ga_2O_3) has emerged as a promising material in semiconductor technology due to its unique electrical and physical properties. This polymorphic material crystallizes in various phases, including α-Ga_2O_3, β-Ga_2O_3, γ-Ga_2O_3, δ-Ga_2O_3, and ϵ-Ga_2O_3, each with distinct crystalline structures, electronic configurations, as well as catalytic and optical properties [15]. The β-Ga_2O_3 phase is the stable form and can be obtained from the other phases or from gallium oxyhydroxide GaOOH through annealing [16, 17]. Ga_2O_3 is highly suited for high-power and high-frequency electronic applications, particularly in demanding environments where thermal stability and high breakdown voltages are required [18,19]. Ga_2O_3 is especially notable for gas sensing, ultraviolet (UV) photodetection, catalysis, and power electronics [20–23]. The interaction between gallium oxide and silica has been studied for various catalytic applications, including the removal of malachite green dye [24], propane dehydrogenation [25], high methane conversion, and enhanced ethane selectivity in hydrocarbon products [26]. This work presents the fabrication of silica matrices with gallium oxide-silica embedded composite through a simple modification of the sol-gel method. A Ga_2O_3 suspension is mixed with TEOS before the hydrolysis process; the modification could be extended to study the use of different types of inorganic or organic materials in suspension to obtain silica composites. We aimed to determine whether gallium oxide can be embedded into a silica matrix during the condensation reaction via the sol-gel method, and we propose this approach as a cost-effective and efficient strategy for producing new hybrid silica-based materials using TEOS. This approach has potential applications in electronics, catalysis, sensors, and optoelectronics. The results obtained in this study demonstrate how the amount of Ga_2O_3 and the number of deposited layers allow the addition of the Ga_2O_3 crystalline structure into the amorphous silica matrix, influencing the morphology.

2. Materials and methods

Gallium oxide (Ga_2O_3) was obtained by thermal conversion of gallium arsenide (GaAs) (111) wafers, approximately 2.5×2.5 cm in size and 300 μm thick, using the annealing process described in reference [27]. The wafers were thermally treated at 800°C and subsequently ground manually using an agate mortar to obtain a powder. A second annealing cycle was applied to remove residual traces of GaAs.

TABLE I. Suspensions of Ga_2O_3 with different concentrations.

Label	Ga_2O_3 powder (g)	Etanol (ml)
C1	0.1	30
C2	0.2	30
C3	0.3	30
C4	0.4	30

The average particle size of the Ga_2O_3 powder, determined by dynamic light scattering (DLS), was approximately 590 nm. The particles exhibited colloidal stability under acidic conditions, as evidenced in Figs. 1a) and 1b). Suspensions were prepared by dispersing Ga_2O_3 powder in ethanol. For each suspension, the mass of powder (as listed in Table I) was mixed with 30 ml of ethanol and stirred at 400 rpm for 10 minutes. Four distinct colloidal concentrations were prepared, as summarized in Table I.

Silica was synthesized by mixing 3.3 ml of tetraethyl orthosilicate (TEOS, Aldrich, 98%) with 3.28 ml of ethanol (EtOH, Fermont, 99.9%), followed by stirring at 650 rpm for 20 minutes to initiate the hydrolysis step. Subsequently, 0.53 ml of deionized water (DI) and 0.001 ml of hydrochloric acid (HCl, Meyer, 36.5-38%) were added, and the mixture was stirred at the same speed for an additional 45 minutes to obtain a homogeneous, transparent sol. The final molar ratio of precursors was 1:2:3.8:3.6$\times 10^{-3}$ (TEOS:DI:EtOH:HCl). A silica matrix was fabricated by drop-casting the solution onto glass substrates without thermal treatment. A layer was formed using three drops ($\sim$ 0.135 ml) then condensation occurred naturally at room temperature. These experimental conditions were used to fabricate a reference sample, labeled as R, formed with three layers. The modification of the silica matrices was made by replacing EtOH with 3.28 ml of a Ga_2O_3 suspension before the condensation reaction (TEOS:DI:EtOH+Ga_2O_3:HCl), which caused the resulting sol to become whitish and turbid. Four different colloidal suspensions (C1, C2, C3, and C4) were used in separate experiments to observe the effect of the suspension concentration. The modified suspensions were deposited onto glass substrates by drop-casting, with 1, 2, 3, or 4 layers each consisting of three drops in 20-second intervals ($\sim$ 0.135 ml per layer). After deposition, the films were left to dry to complete the condensation stage. This deposition method was chosen due to its minimal experimental requirements and compatibility with the sol-gel process for studying Ga_2O_3 embedding during the condensation reaction. No thermal treatment was applied after deposition. Samples with a single layer were translucent, while those with multiple layers exhibited a progressively more intense whitish stain. In thicker films, slight cracking was observed after 12 hours of drying; these culd be attributed to the condensation step, which was made without temperature control. Each sample was labeled using the prefix "M" followed by

two digits: the first indicates the number of deposited layers (1, 2, 3, or 4), and the second denotes the type of colloidal suspension used (C1-C4). For example, sample M33 corresponds to a sample fabricated with three layers using the suspension C3. The hydrodynamic size was measured by Dynamic Light Scattering (DLS) using an Anton Paar Litesizer 500 equipment with a resolution range from 0.3 nm to 10 μm. X-ray measurements were performed using an ULTIMA IV-RIGAKU diffractometer equipped with a Cu anode as a light source (Kα) with $\lambda = 1.546$ Åoperating at 44 kV and 20 mA. 2θ scans were carried out using Bragg-Brentano geometry from 20 to 90° with steps of 0.01°. XRD peak identification was carried out with the Rigaku X-ray Powder Diffraction Software PDXL. The morphology was examined through cross-sectional images obtained with a JEOL JSM 6010LA Scanning Electron Microscope. Micro-Raman measurements were conducted using a Horiba Jobin HR 800 Raman system, with a HeNe excitation source at 632 nm and 50 mW power. Surface charge maps were acquired via EFM using a Park Systems Atomic Force Microscope (AFM) X7, equipped with a Cr-Au-coated tip. Line scan measurements were analyzed using Smart Analysis version 1.4.3 software.

3. Results and discussion

DLS was used to obtain the average particle size and zeta potential of the Ga_2O_3 powder. Figure 1a) shows an average particle size of ∼590 nm; it was assumed that the suspensions have a similar average particle size. The stability of the particles is observed in Fig. 1b), indicating that the particles are stable (low coalescence) in an acidic environment. The structure of the samples was analyzed by XRD, shown in Fig. 2. The pattern of the Ga_2O_3 powder is shown at the bottom of the figures, labeled as P. The powder exhibits a mixed-phase composition, predominantly monoclinic β-Ga_2O_3, with minor contributions from orthorhombic GaOOH. These phases were indexed using PDF cards 00-043-1012 (β-Ga_2O_3) and 00-006-0180 (GaOOH), respectively. A sample of silica without Ga_2O_3 is used as a reference whose XRD pattern is labeled as R; the pattern is consistent with an amorphous silica structure.

The XRD peaks corresponding to β-Ga_2O_3, observed at 30.06° (400), 31.7° (002), 35.18° (111), and 64.48° (-221), are shown in the samples fabricated with colloidal suspensions C3 [Fig. 2a)] and C4 [Fig. 2b)], both with four layers.

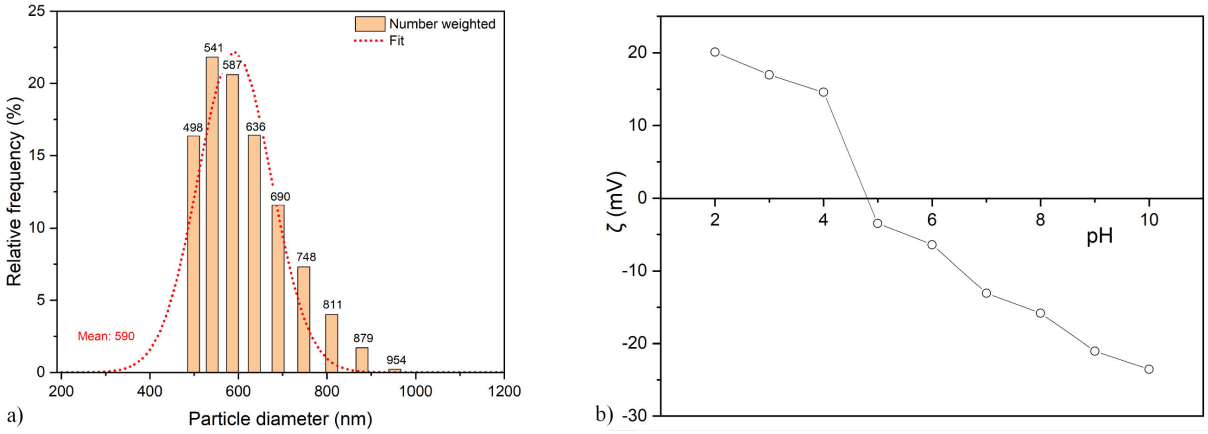

FIGURE 1. Characterization of the Ga_2O_3 powder. a) Average particle size, and b) zeta potential.

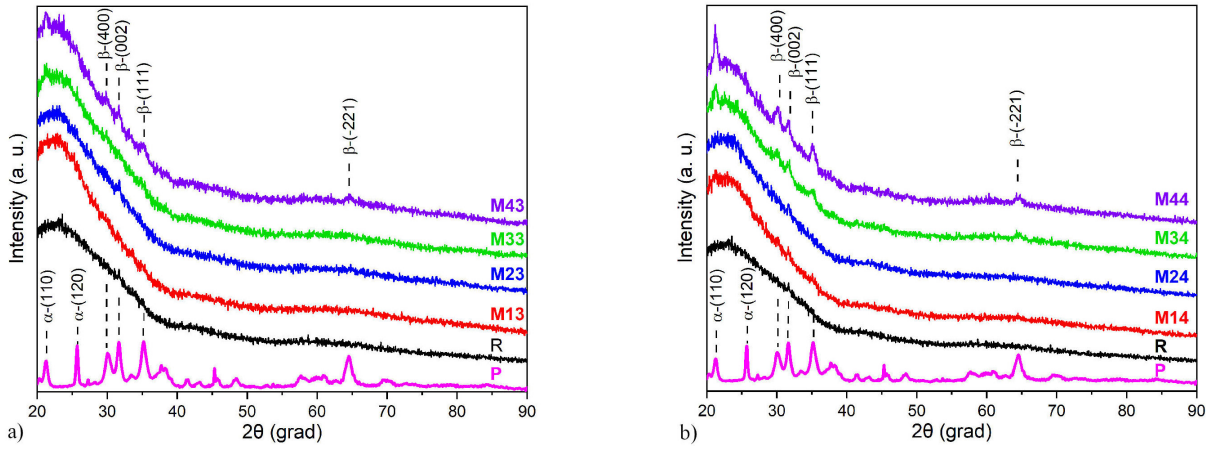

FIGURE 2. XRD patterns of the samples fabricated with colloidal suspensions: a) C3, and b) C4. The labels P and R refer to the Ga_2O_3 powder and the silica reference sample, respectively.

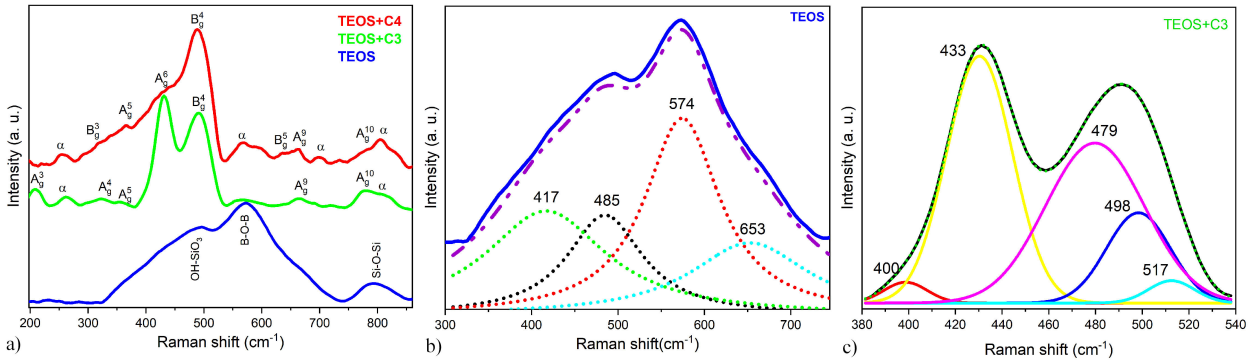

FIGURE 3. Micro-Raman spectra. a) Reference silica sample (bottom) and silica-Ga_2O_3 samples (middle and top), b) Deconvoluted spectrum of reference silica, and c) Deconvoluted spectrum of silica-Ga_2O_3 with C3.

The peaks at 21.5° and 26.4°, corresponding to the (110) and (120) planes of GaOOH (denoted as α-110 and α-120, respectively), were also detected. The presence of these diffraction signals indicates successful incorporation of Ga_2O_3 into the amorphous silica matrix. In contrast, samples fabricated with only one or two layers show significantly weaker β-Ga_2O_3 diffraction signals, close to the background noise level. Furthermore, for samples prepared using colloidal suspensions C1 and C2, the XRD signals corresponding to Ga_2O_3 were too weak to be distinguished from the amorphous silica background and are therefore not shown. The degree of incorporation of the Ga_2O_3-silica composite is reflected in the progressive appearance and intensification of Ga_2O_3-related diffraction peaks within the otherwise amorphous silica pattern. Among all samples, those prepared with colloidal suspension C4 exhibit the most intense peaks, consistent with the higher Ga_2O_3 content in this suspension [Fig. 2b)]. Additionally, an increase in the number of deposited layers correlates with greater peak intensity, further supporting successful incorporation. These results suggest that the extent of Ga_2O_3 incorporation can be tuned by adjusting either the colloidal concentration or the number of deposited layers during the sol-gel process.

Micro-Raman spectroscopy in the range of 200-900 cm^{-1}, was used to observe the vibrational modes of Ga_2O_3 in the samples. The results are presented in Fig. 3, where the label "TEOS" corresponds to the reference sample, whose hydrolysis was performed without modification, while "TEOS+C3" and "TEOS-C4" refer to the samples fabricated by modifying the TEOS hydrolysis with the C3 and C4 suspensions, respectively. The Raman spectrum of the reference sample is shown at the bottom of Fig. 3a). The vibrations at 485 cm^{-1} and 780 cm^{-1} are associated with OH-SiO_3 and Si-O bonds, respectively [27, 28]. A deconvolution of the reference sample (silica) spectrum, from 320-720 cm^{-1}, is shown in Fig. 3b), revealing the vibrational modes at 417, 485, 574, and 653 cm^{-1}. These peaks have been attributed to Si-H (200-500 cm^{-1}), O-C-C (417 cm^{-1}), Si-O-Si (485 cm^{-1}), and O-C2H5 (653 cm^{-1}) bonds related to silica, in addition to B-O and B-O-B bonds (574 cm^{-1}) related to the substrate material (borosilicate) [29, 30]. On the other hand, β-Ga_2O_3 exhibits an optical branch $\Gamma_{\text{opt}} = 10A^g + 4A_u + 5B^g + 8B_u$, of which only the A_g and B_g modes are Raman active [31]. Table II summarizes the β-Ga_2O_3 vibration modes, including those related to GaOOH [32].

The positions of the vibrational peaks are labeled in Fig. 3a) for the Raman spectra of TEOS hydrolysis modified with C3 and C4 suspensions. It is observed that the GaOOH phase increases with the concentration of the colloidal suspension. This result is consistent with the XRD measurements, where the intensity of the (100) GaOOH peak is more pronounced in sample M44 than in sample M43. We assume that during the condensation step, the nucleation GaOOH particles is favored due to the hydroxyl groups promoting the formation of metal-oxygen bonds, allowing the agglomeration of GaOOH particles because it is a metastable phase. On the contrary, β-Ga_2O_3 is a stable phase whose agglomeration rate is lower in the condensation step. A deconvolution of the Raman spectrum of TEOS+C3, in the 380-540 cm^{-1} range, is shown in Fig. 3c). The obtained vibrational modes have

TABLE II. Vibrational modes for β-Ga_2O_3 and GaOOH taken from [31], and [32].

β-Ga_2O_3 cm^{-1}	GaOOH cm^{-1}
A_g^1 - 104.7	201
A_g^2 - 163.5	261
A_g^3 - 202.3	275
A_g^4 - 315.8	320
A_g^5 - 339.7	346
A_g^6 - 420.2	418
A_g^7 - 459.4	433
A_g^8 - 607.1	475
A_g^9 - 656.1	522
A_g^{10} - 757.7	628
B_g^1 - 112.1	653
B_g^2 - 141.3	764
B_g^3 - 348.31	
B_g^4 - 472.8	
B_g^5 - 627.1	

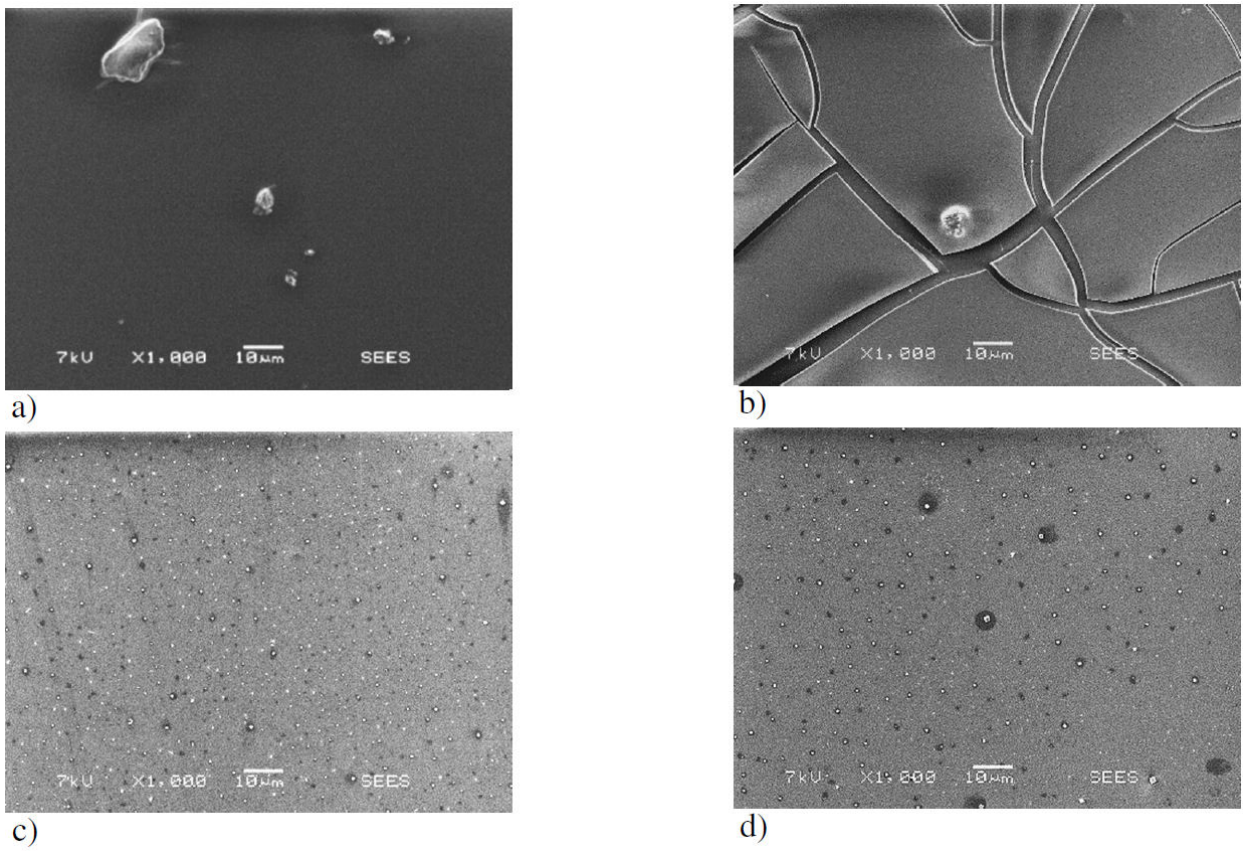

FIGURE 4. SEM micrographs of silica-Ga_2O_3 samples. a) M13, one layer with suspension C3, b) M14, one layer with suspension C4, c) M43, four layers with suspension C3, and d) M44, four layers with colloidal suspension C4.

have been attributed to Ga-OH bonds at 400, 433, 479, 498, and 517 cm^{-1} [33]. The morphology of the samples was analyzed by SEM, as shown in Fig. 4. Samples with one and four layers were selected to illustrate the effects of layer stacking and colloidal concentration on the resulting morphology. In samples with a single layer [Figs. 4a) and 4b)], isolated agglomerates are observed for both colloidal suspensions.

Cracking observed in sample M14 [Fig. 4b)] can be attributed to dry conditions and mechanical handling during sample preparation. With the increasing number of layers [Figs. 4c) and 4d)], the surface exhibits two types of randomly distributed particles, attributed to silica and gallium oxide. EFM was used to map surface charge, leading to the assumption that the brighter particles correspond to Ga_2O_3 or GaOOH rather than silica, since its charge has been reported to be around zero. Then, the brighter particles (charged regions), distributed throughout and between the silica domains (charge around zero regions), are assigned to Ga_2O_3, while the darker regions correspond to silica. These assignments were correlated with DLS (particle size) and z-potential (particle stability) measurements. EFM, which is an electrical imaging mode of the AFM, was employed to map local surface charge distribution. In this technique, the electrostatic interaction between a biased conductive cantilever and the sample surface induces variations in the cantilever's oscillation amplitude and phase, which are recorded to construct an electrostatic amplitude image. During the measurements, an AC modulation bias of 17 kHz with 1 V amplitude was applied between the cantilever and the sample. Topography and amplitude images were acquired in non-contact mode with an additional DC bias of 5 V. The EFM amplitude images (mV) were generated by applying a bias voltage at each pixel, enabling the detection of electric potential gradients across the scanned area.

It is important to observe that the EFM images are blurred because the superficial charge is mapped (mV) instead of the morphology (nm). In EFM, the brighter points regard a higher superficial charge. Meanwhile, the topographic images (AFM) are clear; in this case, the brighter points correspond to the top of the surface. Topography and charge distribution images were measured under standard ambient conditions (temperature and pressure) with a scan area of 20×20 μm. The EFM-AFM images are arranged to show first lineal scans of superficial charge, then, the topography (AFM), and superficial charge areas. Figure 5b) shows the topography of the M14 sample, where some bright particles are visible on the surface top. The corresponding amplitude of the charge distribution is presented in the EFM image of Fig. 5c); the scanned area looks blurry because the superficial charge is shown in morphology instead. EFM images allow us to distinguish between silica and gallium oxide particles by charge difference. Some particles are brighter in the

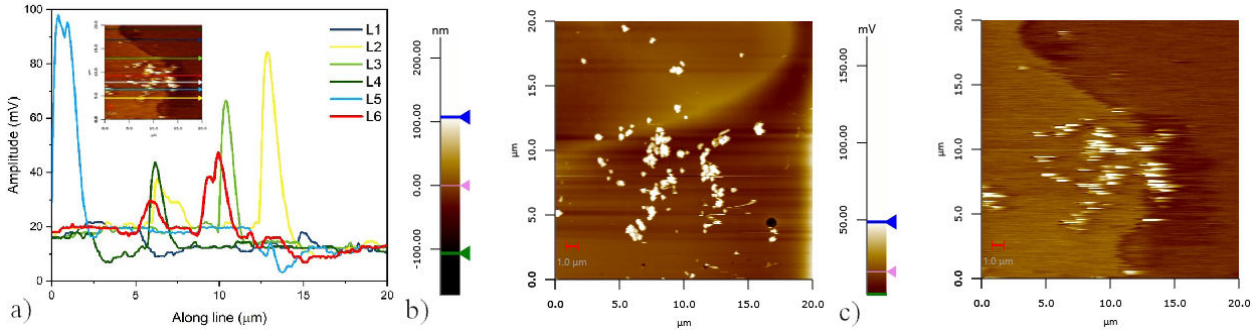

FIGURE 5. EFM (mV) and AFM (nm) obtained on M14 sample. a) Linear scans of charge, b) Topography, and c) EFM amplitude (charge distribution).

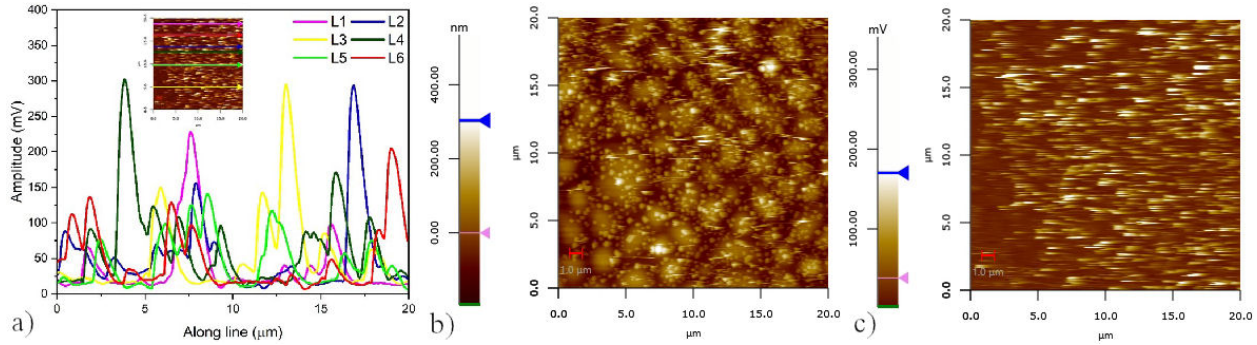

FIGURE 6. EFM (mV) and AFM (nm) obtained on M44 sample. a) Linear scans of charge, b) Topography, and c) EFM amplitude (charge distribution).

topography but not in the EFM, indicating that these particles have a low charge due to the electrical material properties. Silica particles exhibit a surface charge close to zero, depending on their size and roughness, either oxygen or hydrogen, leading to a depletion or accumulation layer on the surface [33,34]. This suggests that the brighter points in EFM correspond to gallium oxide, whose superficial charge is over 20 mV, as observed in Fig. 5a), where several lineal scans were taken on the surface to observe the charge distribution along the scanned line. The topography (AFM) of the M44 sample is shown in Fig. 6b), where semispherical particles are visible. Smaller particles are deposited on and between them, with the brighter particles positioned at the surface. Besides, the EFM image [Fig. 6c)] shows brighter points randomly distributed among dark spots (more obervable at the bottom left). By comparing EFM and AFM it is proposed that the majority of the smaller particles are gallium oxide, while the semispherical particles are silica, on the basis of the observed charge distribution. Lineal scans of charge are presented in Fig. 6a), where charge spots around 300 mV are observed. We assume that this is an effect of stacking layers due to a higher coverage of gallium oxide on the silica particles. In general, the charge amplitude, obtained via EFM, is higher on gallium oxide than on silica particles. The difference on charge allows us to distinguish between the two types of particles. The EFM image mapps only the charge on Ga_2O_3 not the phase.

4. Conclusions

The use of a Ga_2O_3 suspension along the TEOS hydrolysis reaction successfully leads to the embed gallium oxide particles into silica by Sol-gel, resulting in a silica-Ga_2O_3 composite. The functionalization does not require thermal treatment, but its effect on the structure could be studied. The Ga_2O_3 incorporation is evident through the addition of diffraction peaks corresponding to the crystalline gallium oxide, superimposed on the amorphous silica pattern. The results indicate that both the amount of mass in the colloidal suspension and the stacking of deposited layers enhance the intensity of the XRD peaks associated with the crystalline material. Raman characterization further confirms the presence of β-Ga_2O_3 and Ga-OH vibrational modes. We propose that during the condensation step, the nucleation rate of GaOOH particles is higher than that of β-Ga_2O_3 particles, as the hydroxyl groups promote the formation of metal-oxygen bonds, influencing agglomeration. The functionalization process was also characterized by EFM, which revealed higher surface charge distribution, related to gallium oxide or gallium oxyhydroxide particles, compared to the silica particles. The difference in charge, observable in the EFM images, allows us to distinguish silica across the measured areas from the particles added during the hydrolysis reaction in the Sol-gel method, which constitutes a useful application of the AFM. We propose that this work paves the way for func-

tionalizing silica with other semiconductor materials via Sol-gel processes, employing a simple modification of the TEOS with a colloidal suspension to functionalize. This approach represents an innovative method for modifying material properties and creating new hybrid materials, with potential applications in electronics, sensors, and optoelectronics.

Acknowledgments

F. Ramírez-González has a postdoctoral position via the program "Estancias Posdoctorales por México - Modalidad Incidencia" supported by Secretaría de Ciencia, Humanidades, Tecnología e Innovación (SECIHTI).

1. A. A. Nayl *et al*., Recent progress in the applications of silica-based nanoparticles, *RSC Adv.*, **12** (2022) 13706, https://doi.org/10.1039/D2RA01587K
2. L. Mathey *et al*., Functionalization of silica nanoparticles and native silicon oxide with tailored boron-molecular precursors for efficient and predictive p-doping of silicon, *J. Phys. Chem. C*, **119** (2015) 13750, https://doi.org/10.1021/acs.jpcc.5b03408,
3. D. K. Sharma *et al*., Super-Hydrophobic Nanostructured Silica Coating on Aluminum Substrate for Moist Air Condensation. *J. Mat. Eng. Perform.*, **31** (2022) 1266, https://doi.org/10.1007/s11665-021-06254-6
4. K. Koseki *et al*., RAFT polymerization,polymer electrolyte fuel cell,proton conductivity,silica nanoparticle,surface silanol group, *ACS Sustain. Chem. Eng.* **9** (2021) 10093, https://doi/abs/10.1021/acssuschemeng.1c01922
5. X. Jiang *et al*., Synthesis and formation mechanism of amorphous silica particles via sol-gel process with tetraethylorthosilicate, *Ceram. Int.*, **45** (2019) 7673, https://doi/10.1016/j.ceramint.2019.01.067
6. A. Alshahrie, A.A. Al-Ghamdi, and W. Alsayed, The optical and luminescence properties of $Zn_{1-x}Gdx$O ($0 \leq x \leq 0.07$) quantum dots synthesized via tetraethyl orthosilicate assisted colloidal regime for laser diodes application potential, *Optik*, **206** (2020) 163748, https://doi/10.1016/j.ijleo.2019.163748
7. G. A. Molina *et al*., Effects of tetraethyl orthosilicate (TEOS) on the light and temperature stability of a pigment from beta vulgaris and its potential food industry applications, *Molecules*, **19** (2014) 17985, https://doi/10.3390/molecules191117985
8. W. Liu *et al*., Dye-sensitized solar cells,Synthesis,TEOS-assisted,Ultra-small sheets, *Appl. Surf. Sci.*, **313** (2014) 498, https://doi/10.1016/J.APSUSC.2014.06.011
9. J. Yan *et al*., Microstructure and oxidation behavior of SiOC coatings on C/C composites co-deposited with HMDS and TEOS by using CVD process, *Ceram. Int.*, **50** (2024) 7888, https://doi/10.1016/J.CERAMINT.2023.12.117
10. W. Zheng *et al*., Strengthen corrosion resistance of epoxy coating by synergy of oxygen vacancies of CeO_2 nanoparticles as charge capture centers and BTA/TEOS, *Prog. Org. Coat.*, **192** (2024) 108481, https://doi/10.1016/J.PORGCOAT.2024.108481
11. Rimpy, and M. Ahuja, Mechanical properties, Fluconazole-loaded TEOS-modified nanocellulose 3D scaffolds - Fabrication, characterization and its application as vaginal drug delivery system, *J. Drug Deliv. Sci. Technol.*, **75** (2022) 103646, https://doi/10.1016/J.JDDST.2022.103646
12. M. S. Mulla, A. I. Torvi, L. C. Poulose, and M. Y. Kariduraganavar, Development of novel PVA-TEOS-MnO_2 and its PANI incorporated flexible membrane electrodes and evaluation of their supercapacitor performance, *Electrochim. Acta*, **470** (2023) 143260, https://doi/10.1016/J.ELECTACTA.2023.143260
13. R. Ciriminna *et al*., The sol-gel route to advanced silica-based materials and recent applications, *Chem. Rev.*, **113** (2013) 6592, https://doi/10.1021/cr300399c
14. O. Malay, I. Yilgor, and Y. Z. Menceloglu, Effects of solvent on TEOS hydrolysis kinetics and silica particle size under basic conditions, *J. Sol-Gel Sci. Technol.*, **67** (2013) 351, https://doi/10.1007/s10971-013-3088-4
15. A. Oprea, N. Bârsan, and U. Weimar, Work function changes in gas sensitive materials: Fundamentals and applications, *Sens. Actuators, B*, **142** (2009) 470, https://doi/10.1016/j.snb.2009.06.043
16. A. Devamanoharan *et al*., Investigating Stable Low-Energy Gallium Oxide (Ga_2O_3) Polytypes: Insights into Electronic and Optical Properties from First Principles, *ACS Omega*, **9** 2024 16207, https://doi/10.1021/acsomega.3c10192
17. X. Liu *et al*., Gallium oxide nanorods by the conversion of gallium oxide hydroxide nanorods, *J. Alloys. Compd.*, **439** (2007) 275, https://doi/10.1016/J.JALLCOM.2006.08.062
18. J. Debdeep, Gallium Oxide Materials Properties, Crystal Growth, and Devices, 1st edition. (Springer, Cham, 2020), pp. 739-754 https://doi.org/10.1007/978-3-030-37153-1
19. K. Sato *et al*., High-temperature operation of gallium oxide memristors up to 600 K, *Scientific Reports*, **13** (2023) 1261, https://doi/10.1038/s41598-023-28075-4
20. J. Zhu *et al*., Gallium Oxide for Gas Sensor Applications: A Comprehensive Review, *Materials*, **15** (2022) 7339, https://doi.org/10.3390/ma15207339Academic
21. L. Wang *et al*., Recent Progress in Solar-Blind Photodetectors Based on Ultrawide Bandgap Semiconductors, *ACS Omega*, **9** (2024) 25429, https://doi/10.1021/acsomega.4c02897
22. W. Lueangchaichaweng *et al*., Gallium oxide nanorods: novel, template-free synthesis and high catalytic activity in epoxidation reactions, *Angew. Chem. Int. Ed.*, **53** (2014) 1585, https://doi/10.1002/ange.201308384

23. A. J. Green *et al.*, β-Gallium oxide power electronics, *APL Materials*, **10** (2022) 029201, https://doi/10.1063/5.0060327

24. R. A. El-Salamony, and R. E. Morsi, Stable gallium oxide@ silica/polyvinyl pyrrolidone hybrid nanofluids: Preparation, characterization, and photo-activity toward removal of malachite green dye, *J. Mol. Liq.*, **271** (2018) 589, https://doi/10.1016/j.molliq.2018.08.139

25. I. Takahara *et al.*, Effects of pre-treatment of a silica-supported gallium oxide catalyst with H_2 on its catalytic performance for dehydrogenation of propane, *Catal. Lett.*, **96** (2004) 29, https://doi/10.1023/B:CATL.0000029525.33197.89

26. L. Yuliati *et al.*, Photocatalytic nonoxidative coupling of methane on gallium oxide and silica-supported gallium oxide, *J. Catal.*, **257** (2008) 396, https://doi/10.1016/j.jcat.2008.05.022

27. C. A. M. Mulder, and A. A. J. M. Damen, The origin of the "defect" 490 cm^{-1} Raman peak in silica gel, *J. Non-Cryst. Solids*, **93** (1987) 387, https://doi/10.1016/S0022-3093(87)80183-7

28. S. B. Khemis *et al.*, Structural analysis of sputtered amorphous silica thin films: A Raman spectroscopy investigation, *Thin Solid Films*, **733** (2021) 138811, https://doi/10.1016/j.tsf.2021.138811

29. D. Manara, A. Grandjean, and D. R. Neuville, Advances in understanding the structure of borosilicate glasses: A Raman spectroscopy study, *Am. Mineral.*, **94** (2009) 777, https://doi/10.2138/am.2009.3027

30. O. N. Koroleva, L. A. Shabunina, and V. N. Bykov, Structure of borosilicate glass according to Raman spectroscopy data, *Glass and Ceramics*, **67** (2011) 340, https://doi/10.1007/s10717-011-9293-0

31. B. Liu, M. Gu, and X. Liu, Lattice dynamical, dielectric, and thermodynamic properties of β-Ga_2O_3 from first principles, *Appl. Phys. Lett.*, **91** (2007) 3, https://doi/10.1063/1.2800792

32. Y. Zhao, and R. L. Frost, Raman spectroscopy and characterisation of α-gallium oxyhydroxide and β-gallium oxide nanorods, *J. Raman Spectrosc.*, **39** (2008) 1494, https://doi/10.1002/jrs.2028

33. M. Barisik *et al.*, Size dependent surface charge properties of silica nanoparticles, *J. Phys. Chem. C*, **118** (2014) 1836, https://doi/10.1021/jp410536n

34. B. O. Alan, M. Barisik, and H. G. Ozcelik, Roughness Effects on the Surface Charge Properties of Silica Nanoparticles, *J. Phys. Chem. C*, **124** (2020) 19327455, https://doi/10.1021/acs.jpcc.0c00120

35. A. Y. Polyakov *et al.*, Impact of Hydrogen Plasma on Electrical Properties and Deep Trap Spectra in Ga_2O_3 Polymorphs, *Crystals*, **13** (2023) 1400, https://doi/10.3390/CRYST13091400

36. F. Shi, and H. Qiao, Preparations, properties and applications of gallium oxide nanomaterials - A review, *Nano Select*, **3** (2022) 348, https://doi/10.1002/nano.202100149

37. J. E. N. Swallow *et al.*, Transition from electron accumulation to depletion at β-Ga_2O_3 surfaces: The role of hydrogen and the charge neutrality level, *APL Materials*, **7** (2019) 022528, https://doi/10.1063/1.5054091